Chinese Chemical Letters 33 (2022) 1390–1394

Contents lists available at ScienceDirect

Chinese Chemical Letters

journal homepage: www.elsevier.com/locate/cclet

H_2S-assisted growth of 2D MS_2 (M = Ti, Zr, Nb)

Yiwei Zhang[a], Peng Zhang[a,*], Tengfei Xu[b], Xingguo Wang[a], Huaning Jiang[a], Yongji Gong[a,*]

[a] School of Materials Science and Engineering, Beihang University, Beijing 100191, China
[b] State Key Laboratory of Infrared Physics, Shanghai Institute of Technical Physics, Chinese Academy of Sciences, Shanghai 200083, China

ARTICLE INFO

Article history:
Received 12 June 2021
Revised 7 July 2021
Accepted 13 July 2021
Available online 8 September 2021

Keywords:
Chemical vapor deposition
Growth mechanism
2D transition-metal dichalcogenides
Titanium disulfide
FET properties

ABSTRACT

2D transition metal dichalcogenides (TMDCs) have drawn an enormous amount of attention due to their fascinating properties and application potential in next-generation information process and storage. However, the lack of proper synthesis approach limits their application. Here, we report a controllable synthesis method to grow ultrathin MS_2 (M = Ti, Nb, Zr) nanosheets with H_2S-assisted chemical vapor deposition (CVD). We found that the presence of H_2S plays an important role to control the morphology of nanosheets including the lateral size and the nucleation density. With the assistance of H_2S, the growth of MS_2 shows much thinner thickness with largely decreased nucleation density, beneficial for the device application, which can be attributed to the kinetics dominated growth. Our method hence opens a new avenue for the CVD growth of 2D TMDCs and the corresponding heterojunction, and paves the way for exploring their intriguing properties and applications.

Two-dimensional (2D) transition metal dichalcogenides (TMDCs) are layered materials with fascinating properties, like the quantum spin Hall effect [1], valley polarization [2] as well as a wide range of potential applications [3], like field-effect transistors [4,5], photodetectors [6] and functional devices [7,8]. Among them, the growth of semiconducting VIB group TMDCs such as MoS_2 and WSe_2 has been well realized and their applications in various fields have been systematically studied [9–13]. In contrast, the growths of some metallic or narrow band-gap 2D materials with promising properties are still in their infancy. Titanium disulfide (TiS_2) and niobium disulfide (NbS_2), for example, have attracted increasing interests for their devisable electronic properties [14–18] and show application potentials as promising localized surface plasmon resonance materials [19] and superconductors. Another example, zirconium disulfide (ZrS_2) with a smaller band gap than MoS_2 displays high carrier mobility and unusual electronic properties [20], which brings the potential applications in nanoelectronics [21] and photodetectors [22–24]. However, many issues are remained to be tackled in the controllable synthesis of these ultrathin TMDCs nanosheets.

Several top-down methods, such as mechanical exfoliation [25], electrochemical lithium intercalation exfoliation and liquid sonication exfoliation [26,27], illustrate considerable handleability in the preparation of typical TMDs, black phosphorus (BP). However, it is usually difficult to control the shape, lateral size and thickness of the obtained nanosheets [28,29]. Recently, bulk layered compounds [30] or large-size [31] TiS_2 flakes can be synthesized by chemical vapor transport (CVT) technique or a mixed-method of physical vapor deposition (PVD) and electron beam evaporation. Meanwhile, it is reported some substrates, such as h-BN and transferred graphene, are applied to synthesize ultrathin 2D nanocrystal by CVD [32,33]. Nevertheless, the uniformity of the as-grown samples and the repeatability of these approaches are still not very satisfactory.

Herein, we report a highly reproducible synthesis of MS_2 (M = Ti, Nb, Zr) nanosheets using H_2S-assisted CVD. By adjusting the growth parameters, like the growth temperature and the H_2S flow rate, the size and thickness of the flakes can be well controlled. Various characterization techniques confirm the high quality of the as-synthesized MS_2 nanosheets and FET devices based on TiS_2 nanosheets show narrow band-gap semiconductor behavior and a thickness-dependent resistance.

The layers of MS_2 (M = Ti, Nb, Zr) are stacked *via* relatively weak van der Waals interactions. In each layer, M (M = Ti, Nb, Zr) atoms are sandwiched by six sulfur atoms. Fig. 1a shows the schematics of the growth of MS_2 (M = Ti, Nb, Zr) films on SiO_2/Si substrates *via* a CVD system together with the typical atomic structure of obtained MS_2 (M = Ti, Nb, Zr) from the side-view. More details about the growth process and experimental setup are provided in the Experimental Section and Fig. S1 (Supporting information). Briefly, sulfur powder and MO_x/NaCl mixture were used as the reactants, where NaCl powder can help to decrease the en-

* Corresponding authors.
E-mail addresses: x_l_zhang@buaa.edu.cn (P. Zhang), yongjigong@buaa.edu.cn (Y. Gong).

https://doi.org/10.1016/j.cclet.2021.07.036
1001-8417/

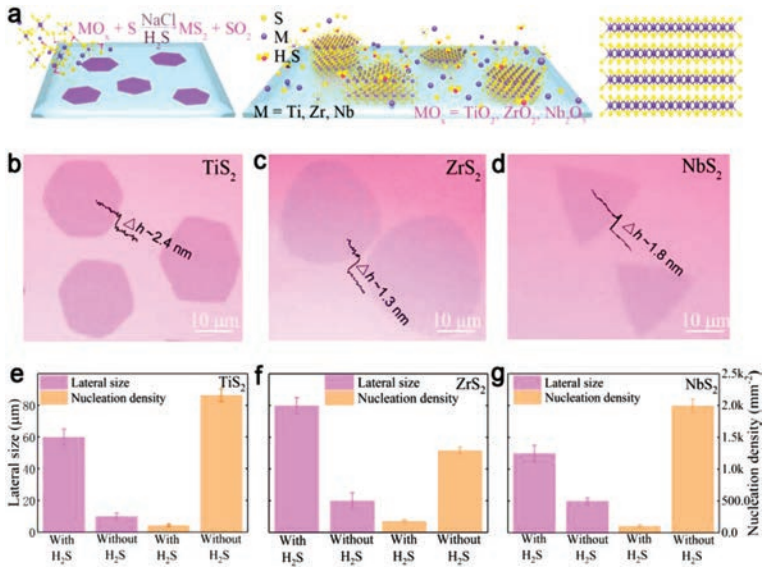

Fig 1. Synthesis of MS_2 (M = Ti, Nb, Zr) nanosheets. (a) Schematic illustration of MS_2 synthesis. (b-d) Typical OM images of MS_2 nanosheets grown on SiO_2/Si substrates with the corresponding height line profiles. (e-g) Sample statistical graphs of the lateral size and nucleation density of products grown with or without the assistance of H_2S.

ergy barrier for the reaction and thus increase the growth rate [34]. Ar is used as carrier gas and H_2S is introduced only at the high temperature around 800 °C for about 3 min to get ultrathin nanosheets. The typical optical microscopy (OM) images of as-grown MS_2 (M = Ti, Nb, Zr) nanosheets with H_2S-assistance are displayed in Figs. 1b-d, where the as-synthesized samples display obvious contrast with the SiO_2/Si substrates. The height profiles in Figs. 1b-d show a smooth surface with the thickness of ~2.4 nm for TiS_2, ~1.3 nm for ZrS_2 and ~1.8 nm for NbS_2, respectively. And their corresponding AFM height images of the representative MS_2 (M = Ti, Nb, Zr) nanosheets are listed as Fig. S2 (Supporting information). Furthermore, the effect of H_2S on the nucleation density and lateral size of these three kinds of samples are shown in Figs. 1e-g. As shown, the presence of H_2S can significantly reduce the nucleation density of TiS_2, ZrS_2 and NbS_2, thus, leading to much increased lateral size of the products.

To find the optimal conditions for the growth of TiS_2 nanosheets, synthesis temperature and H_2S flow are investigated in detail (Fig. 2). Keeping the other growth parameters (growth time, carrier gas, precursor quantity, *etc.*) constant, H_2S as auxiliary gas can obviously reduce the nucleation density and increase the lateral size of the samples compared to the growth without using H_2S. Figs. 2a-d show the typical OM images of TiS_2 grown from 750 °C to 900 °C without the help of H_2S, where the thickness increases and the lateral size changes little with increased growth temperature. Figs. 2e-h display the revolution of typical OM images of TiS_2 grown with 2 sccm H_2S from 750 °C to 900 °C, in which the lateral size increases first and then the thickness becomes thicker. The corresponding statistical histogram of the number of layers increasing with temperature can be seen in Fig. S3 (Supporting information). The statistical histograms of the lateral size and nucleation density in Figs. 2i and j show the effect of H_2S clearly. The lateral size of TiS_2 nanosheets increases from ~5 μm to ~50 μm when introducing H_2S while the nucleation density decreases from ~3k mm^{-2} to ~0.5k mm^{-2}. In addition, the change of lateral size with different temperature is observed, which may be caused by the kinetic and thermodynamic process including the source sublimation rate, the nucleation rate, the growth rate and the stability of the products [35,36]. At relatively low temperature, the growth process is largely kinetically controlled [37]. With higher concentration of the reactants vapor at a little bit higher temperature, the

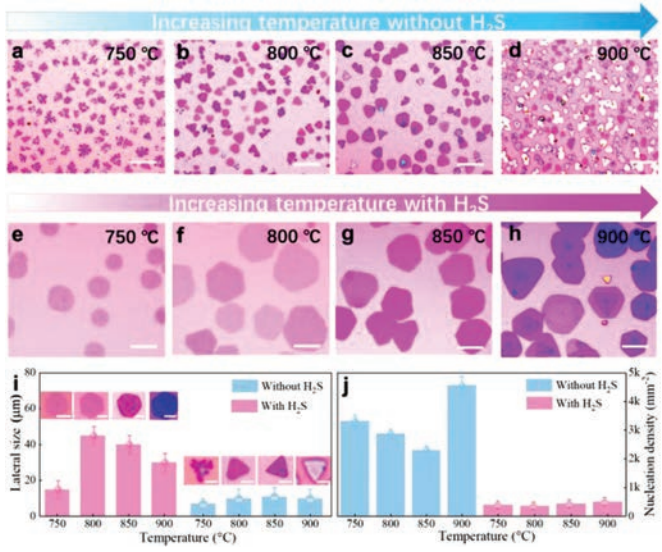

Fig 2. Typical OM images of TiS_2 flakes grown under different conditions. OM images of TiS_2 nanosheets grown without H_2S at (a) 750 °C, (b) 800 °C, (c) 850 °C, (d) 900 °C, respectively. OM images of TiS_2 nanosheets grown with the assistance of H_2S at (e) 750 °C, (f) 800 °C, (g) 850 °C, (h) 900 °C, respectively. (i) The lateral size as a function of the growth temperature with the corresponding OM images. (j) Nucleation density of TiS_2 flakes as a function of the growth temperature. Scale bars in (a-i): 10 μm.

product will prefer to deposit on the edge with high activity, which will lead to lateral growth. However, the growth is more thermodynamically controlled with further increased temperature, which will lead to thicker samples. Also, the supersaturated vapor source tends to increase the nucleation rate. As a result, the nanosheets tend to be thicker and smaller. However, the introduction of H_2S could promote the growth of TiS_2 in the lateral dimension from both thermodynamics and kinetics, which will be discussed in detail in the following part. The above experimental results confirm that ideal ultrathin TiS_2 nanosheets could be gained at 800 °C with the assistance of H_2S. The same research methods are used to the synthesis of ZrS_2 and NbS_2 and the characterization of the as-

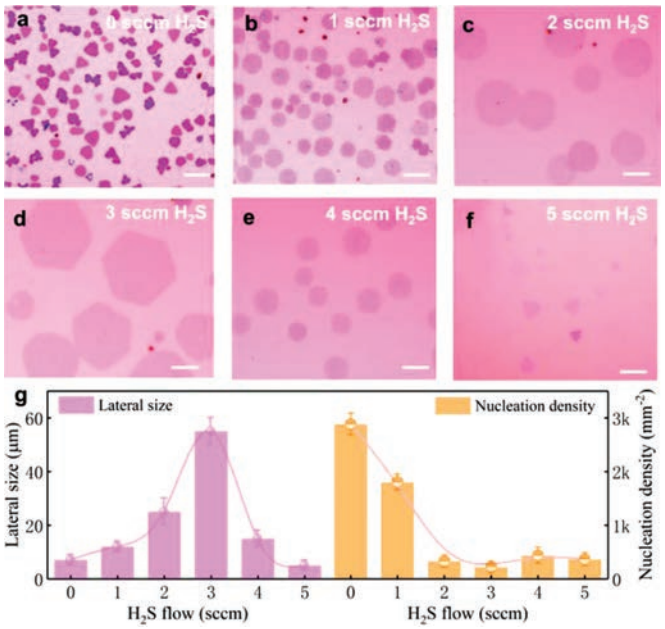

Fig 3. The effect of the flow rate of H_2S on growing TiS_2 nanosheets at 800 °C. (a-f) OM images of TiS_2 nanosheets grown with H_2S flow range from 0 to 5 sccm. All scale bars are 10 μm. (g) TiS_2 lateral size and nucleation density as a function of the H_2S flow rate.

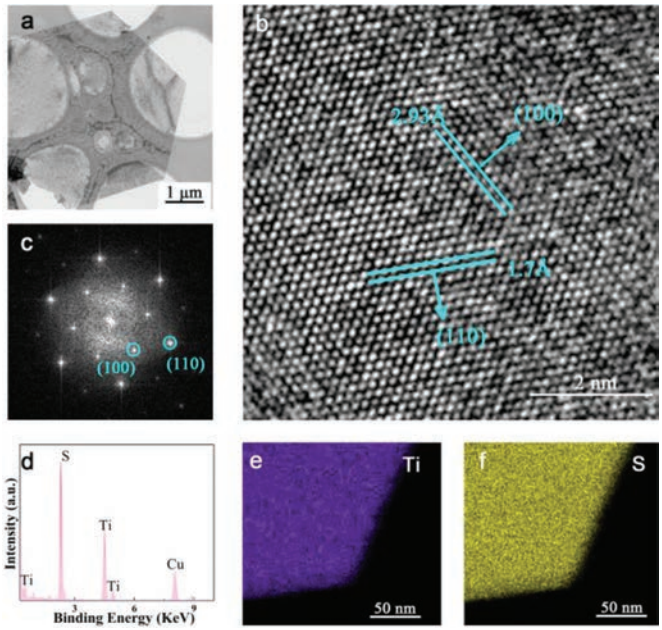

Fig 5. TEM characterization of the as-grown TiS_2. (a) Low-magnification TEM image of TiS_2 nanosheets. (b) The high-resolution TEM image. (c) The corresponding fast Fourier transform (FFT) image. (d) Representative EDS spectrum for the as-grown TiS_2 and the corresponding elemental mapping images of Ti (e) and S (f) elements.

grown nanosheets can be seen in Supporting information (Figs. S4 and S5), showing similar effects of H_2S on the morphology control.

To deeply understand the mechanism of how H_2S critically affects the synthesis of TiS_2 nanosheets, the effect of H_2S flow rate on the reaction is studied in detail. Figs. 3a-f illustrate the OM images of TiS_2 grown at 800 °C with different H_2S/Ar flow rate. Obviously, the nucleation density and domain size are very sensitive to H_2S flow rate. With the increase of H_2S flow, the lateral size firstly increases and then decreases while its nucleation density firstly decreases and then keeps constant. Thus, 3 sccm H_2S flow rate is the best condition that can get the maximum size of TiS_2 nanosheets (about 60 μm). The experimental phenomenon shows that a small H_2S flow can significantly decrease the nucleation density (Fig. 3g), which is beneficial for achieving a large domain size at the proper growth time and growth temperature. A simple growth mechanism model and typical OM images of TiS_2

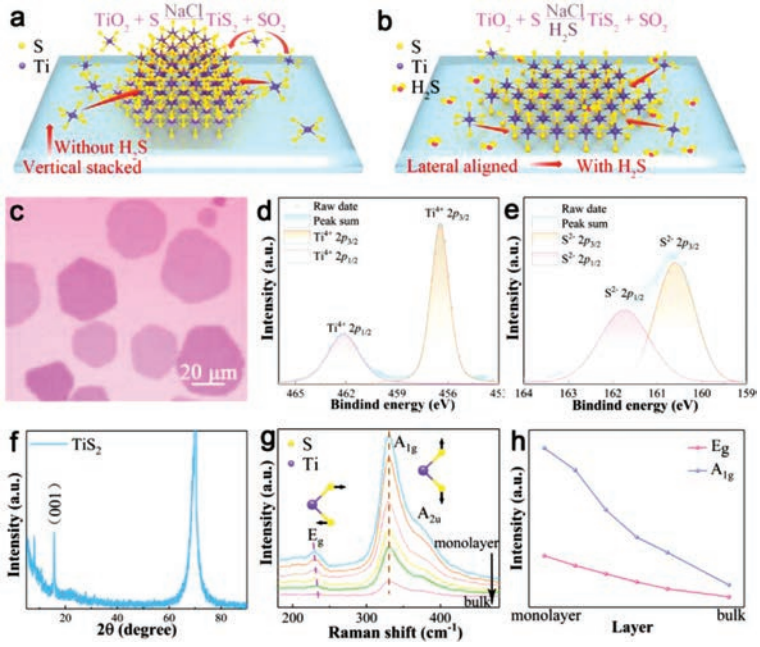

Fig 4. Phase characterizations of the as-grown TiS_2. (a, b) Possible growth models of TiS_2 nanosheets on SiO_2/Si substrates. (c) Typical OM image of TiS_2 films grown with 3 sccm H_2S. (d, e) XPS characterization of Ti 2p and S 2p peaks of the as-grown TiS_2 sample. (f) The XRD pattern of the TiS_2 films flakes on SiO_2/Si from a thick sample. (g) Raman spectrum of TiS_2 nanosheets with different layers using a 532 nm excitation laser (including a representation of A_{1g} and E_g vibrational modes). The dashed line in E_g highlights a minor change of the peak position. (h) Peak intensity change of the A_{1g} and E_g vibrational mode as a function of layer numbers.

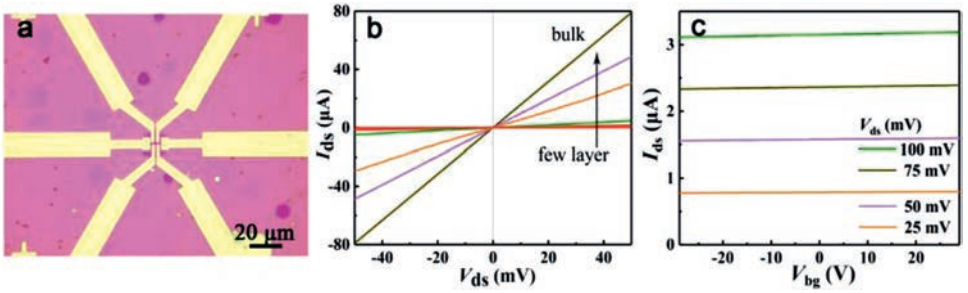

Fig 6. Electrical measurement of the TiS_2 nanosheets. (a) The OM image of a fabricated device based on TiS_2 grown on SiO_2/Si substrate. (b) I_{ds}-V_{ds} curve of the TiS_2 device collected at room temperature. (c) The transfer characteristic curves of the devices.

nanosheets are speculated in Figs. 4a-c. Firstly, compared to S, H_2S could help to produce more active Ti intermediate products with higher Gibbs free energy, which could further lower the ΔG of the reaction. This will further minimize the thermodynamic stability difference of the lateral growth product and vertical growth product. In this case, the dynamics will play a more dominant role and the source atoms will quickly add to the edge sites to realize the lateral growth [37]. Secondly, the high activity of H_2S can react with the TiO_2/NaCl powder before its evaporation, this could decrease the vapor pressure of Ti species to obtain a low nucleation density. Thus, further increasing the flow rate of H_2S will inhibit the growth of TiS_2 on the substrate.

X-ray photoelectron spectroscopy (XPS) was further conducted to study the chemical states and elemental composition of the as-grown samples. As Figs. 4d and e shown, the chemical states of Ti^{4+} $2p_{3/2}$ and $2p_{1/2}$ can be identified from the peaks at ~456 and 462 eV (Fig. 4d) and the peaks at ~160 and ~162 eV (Fig. 4e) correspond to the $2p_{3/2}$ and $2p_{1/2}$ states of S, respectively. The elemental composition of Ti:S perfectly matches the stoichiometric ratio of 1:2.

X-ray diffraction (XRD) characterization was performed on a thick sample to further identify the crystal structure of the as-grown samples. As shown in Fig. 4f, the peak at $2\theta = 15.56°$ of the CVD-grown sample matches well with the (001) crystal planes of TiS_2 reported in the literature [29,38]. The peak at $2\theta = 69°$ can be indexed to the Si substrates. Raman characterization with 532 nm laser is further applied to characterize the grown samples, as shown in Fig. 4g. It shows a peak at ~230 cm^{-1} ascribed to the in-plane E_g, a peak at ~330 cm^{-1} corresponding to out-of-plane A_{1g} modes, and a shoulder mode at about 375 cm^{-1} assigned to A_{2u}, which is consistent with reported literature of TiS_2 [29]. When the thickness increases, the E_g peak exhibits a blueshift from 228 cm^{-1} (monolayer) to 236 cm^{-1} (bulk) while the A_{1g} peak at ~330 cm^{-1} shows a negligible shift. Fig. 4h further summarizes the evolution of Raman intensities with thickness, showing decreased intensity of both E_g and A_{1g} peaks with increased thickness.

Further, transmission electron microscope (TEM) was performed on the transferred samples to investigate the detailed atomic structures of TiS_2 samples. The low-magnification TEM image (Fig. 5a) shows a typical TiS_2 flake on the lacey carbon films supported by Cu grids. Fig. 5b shows a high-resolution TEM (HRTEM) image of the sample, displaying a good atomic arrangement. The lattice spacing of ~1.70 and ~2.93 Å matches the predicted spacing for the (110) and (100) planes of 1T-TiS_2. The corresponding fast Fourier transformation (FFT) image (Fig. 5c) presents only one set of hexagonal diffraction spots, which confirms the single-crystal nature and high crystal quality. Energy dispersive spectroscopy (EDS) employed along with TEM on the transferred samples identifies the chemical composition of ~1:2 for Ti:S in Fig. 5d. The EDS maps (Figs. 5e and f) clearly exhibit the spatial distribution of Ti and S atoms and their uniform color distribution demonstrates the compositional uniformity of the synthesized TiS_2 nanosheet. Together, these TEM results confirm that the H_2S-assisted CVD method can obtain ultrathin single-crystal TiS_2 nanosheets with high quality.

In addition, electrical measurements were performed on a series of FETs based on the as-grown TiS_2 samples with different thickness. Fig. 6a exhibits the OM image of a typical fabricated device with a channel width (W) of 8 μm and channel length (L) of 7 μm. The Ti/Au electrodes were made directly on the samples using photolithography and e-beam metal deposition (more details are provided in the Experimental Section in Supporting information). Fig. 6b shows the thickness-dependent resistance of TiS_2 devices, exhibiting that the resistance decreases with the increase of thickness. The corresponding linear current-voltage (I_{ds}-V_{ds}) curve collected at room temperature also demonstrates an Ohmic contact at the interface. The transfer characteristic curves of the devices under different V_{ds} in Fig. 6c demonstrate the narrow band-gap semiconductor behavior of the TiS_2 channel [39,40].

In summary, we have introduced H_2S to assist the synthesis of several 2D transition-metal dichalcogenide materials, such as TiS_2, NbS_2 and ZrS_2, in an ambient pressure CVD system. Further XRD, TEM and Raman characterizations reveal that the nanosheets are single crystals and possess high crystallinity. We take TiS_2 as an example to study the role of the H_2S in the growth, where H_2S can effectively inhibit the growth in the vertical direction and reduce the nucleation density due to its high reactivity. The method provides direct access to highly crystalline TiS_2, ZrS_2 and NbS_2 nanosheets, with superior controllability over the growth morphologies, such as the domain size and thickness. Our study hence suggests a promising CVD paradigm to synthesize high quality various 2D atomic crystals. It also provides a possible inspiration for the preparation of other 2D TMDCs and opens up opportunities for exploring a variety of intriguing physics, corresponding properties and applications of 2D TMDCs.

Declaration of competing interest

The authors declare that they have no known competing financial interests or personal relationships that could have appeared to influence the work reported in this paper.

Acknowledgments

This work was supported by the National Key R&D Program of China (No. 2018YFA0306900) and the National Natural Science Foundation of China (No. 51872012).

Supplementary materials

Supplementary material associated with this article can be found, in the online version, at doi:10.1016/j.cclet.2021.07.036.

References

[1] X.F. Qian, J.W. Liu, L. Fu, J. Li, Science 346 (2014) 1344–1347.
[2] H. Zeng, J. Dai, W. Yao, D. Xiao, X. Cui, Nat. Nano. 7 (2012) 490–493.
[3] H. Que, H. Jiang, X. Wang, et al., Acta Phys. Chim. Sin. 37 (2021) 2010051.
[4] B. Radisavljevic, A. Kis, Nat. Mater. 12 (2013) 815–820.
[5] H. Zhang, ACS Nano 9 (2015) 9451–9469.
[6] C. Xie, C. Mak, X. Tao, F. Yan, Adv. Funct. Mater. 27 (2017) 1603886.
[7] Q.H. Wang, K. Kalantar-Zadeh, A. Kis, J.N. Coleman, M.S. Strano, Nat. Nano. 7 (2012) 699–712.
[8] X. Wang, L. Meng, B. Li, Y. Gong, Mater. Today. 47 (2021) 108–130.
[9] L. Zhang, G. Wang, Y. Zhang, et al., ACS Nano 14 (2020) 10265–10275.
[10] L. Meng, Y. Ma, K. Si, et al., Tungsten 1 (2019) 46–58.
[11] Y. Chen, S. Lan, M. Zhu, Chin. Chem. Lett. 32 (2021) 2052–2056.
[12] J. Tan, J. Hu, J. Ren, et al., Chin. Chem. Lett. 31 (2020) 2103–2108.
[13] Y. Feng, L. Ding, D. Ji, L. Wang, W. Guo, Chin. Chem. Lett. 29 (2018) 892–894.
[14] M.S. Whittingham, Science 192 (1976) 1126–1127.
[15] J. Ĉaja, R.B. Kaner, A.G. MacDiarmid, J. Electrochem. Soc. 131 (2019) 2744–2750.
[16] C. Xu, P.A. Brown, K.L. Shuford, RSC Adv 5 (2015) 83876–83879.
[17] Y. Zhang, L. Yin, J. Chu, et al., Adv. Mater. (2018) 1803665.
[18] P. Zhang, C. Bian, J. Ye, et al., Sci. China Mater. 63 (2020) 1548–1559.
[19] Z. Zhu, Y. Zou, W. Hu, et al., Adv. Funct. Mater. 26 (2016) 1793–1802.
[20] H. Zhai, Z. Qin, D. Sun, et al., Phys. Chem. Chem. Phys. 20 (2018) 23656–23663.
[21] Y. Zhu, X. Wang, M. Zhang, C. Cai, L. Xie, Nano Res. 9 (2016) 2931–2937.
[22] X. Wang, L. Huang, X.-W. Jiang, et al., J. Mater. Chem. C. 4 (2016) 3143–3148.
[23] M. Mattinen, G. Popov, M. Vehkamäki, et al., Chem. Mater. 31 (2019) 5713–5724.
[24] Y. Wang, Z. Geng, RSC Adv 6 (2016) 58325–58328.
[25] G.H. Lee, Y.J. Yu, X. Cui, et al., ACS Nano 7 (2013) 7931–7936.
[26] X. Sun, B. Shi, H. Wang, et al., Adv. Opt. Mater. 8 (2019) 1901181.
[27] Y. Liu, X. Li, E. Wang, et al., Appl. Surf. Sci. 541 (2021) 148371.
[28] X. Cai, Y. Luo, B. Liu, H.M. Cheng, Chem. Soc. Rev. 47 (2018) 6224–6266.
[29] P.C. Sherrell, K. Sharda, C. Grotta, et al., ACS Omega 3 (2018) 8655–8662.
[30] A. Chaturvedi, P. Hu, V. Aravindan, C. Kloc, S. Madhavi, J. Mater. Chem. A. 5 (2017) 9177–9181.
[31] Y. Li, A. Singh, K. Reidy, et al., Adv. Funct. Mater. 30 (2020) 2003617.
[32] Z. Li, W. Yang, Y. Losovyj, et al., Nano Res 11 (2018) 5978–5988.
[33] H. Bark, Y. Choi, J. Jung, et al., Nanoscale 10 (2018) 1056–1062.
[34] J. Zhou, J. Lin, X. Huang, et al., Nature 556 (2018) 355–359.
[35] B. Zhao, W. Dang, Y. Liu, et al., J. Am. Chem. Soc. 140 (2018) 14217–14223.
[36] L. Meng, Z. Zhou, M. Xu, et al., Nat. Commun. 12 (2021) 809.
[37] X. Wang, Z. Zhou, P. Zhang, et al., Chem. Mater. 32 (2020) 2321–2329.
[38] S.J. Varma, J. Kumar, Y. Liu, et al., Adv. Opt. Mater. 5 (2017) 1700713.
[39] Z. Gao, Q. Ji, P.C. Shen, et al., ACS Appl. Mater. Interfaces. 10 (2018) 34401–34408.
[40] G.H. Han, D.L. Duong, D.H. Keum, S.J. Yun, Y.H. Lee, Chem. Rev. 118 (2018) 6297–6336.